Eur. Phys. J. A **15**, 303–314 (2002)
DOI 10.1140/epja/i2002-10037-5

THE EUROPEAN PHYSICAL JOURNAL A

K^+ production in proton-nucleus reactions and the role of momentum-dependent potentials

Z. Rudy[1], W. Cassing[2,a], L. Jarczyk[1], B. Kamys[1], and P. Kulessa[3,4]

[1] M. Smoluchowski Institute of Physics, Jagellonian University, PL-30059 Cracow, Poland
[2] Institut für Theoretische Physik, Justus Liebig Universität Giessen, D-35392 Giessen, Germany
[3] Institut für Kernphysik, Forschungszentrum Jülich, D-52425 Jülich, Germany
[4] W. Niewodniczański Institute of Nuclear Physics, PL-31342, Cracow, Poland

Received: 28 January 2002 /
Published online: 19 November 2002 –
Communicated by P. Schuck

Abstract. The production of K^+-mesons in proton-nucleus collisions from 1.0 to 2.5 GeV is analyzed with respect to one-step nucleon-nucleon ($NN \to NYK^+$) and two-step Δ-nucleon ($\Delta N \to K^+YN$) or pion-nucleon ($\pi N \to K^+Y$) production channels on the basis of a coupled-channel transport approach (CBUU) including the kaon final-state interactions. The influence of momentum-dependent potentials for the nucleon, hyperon and kaon in the final state are studied as well as the importance of K^+ elastic rescattering in the target nucleus. The transport calculations are compared to the experimental K^+ spectra taken at LBL Berkeley, SATURNE, CELSIUS, GSI and COSY-Jülich. It is found that the momentum-dependent baryon potentials affect the excitation function of the K^+ cross-section; at low bombarding energies of ~ 1.0 GeV the attractive baryon potentials in the final state lead to a relative enhancement of the kaon yield, whereas the net repulsive potential at bombarding energies ~ 2 GeV causes a decrease of the K^+ cross-section. Furthermore, it is pointed out that especially the K^+ spectra at low momenta (or kinetic energy T_K) allow to determine the in-medium K^+ potential almost model independently due to a relative shift of the K^+ spectra in kinetic energy that arises from the acceleration of the kaons when propagating out of the nuclear medium to free space, *i.e.* converting the potential energy to the kinetic energy of the free kaon.

PACS. 13.60.Le Meson production – 13.75.Jz Kaon-baryon interactions – 14.40.Aq π, K, and η mesons – 25.40.-h Nucleon-induced reactions

1 Introduction

The production of mesons heavier than pions in $p + A$ reactions at bombarding energies far below and close to the free nucleon-nucleon threshold is of specific interest [1–18] as one hopes to learn either about cooperative nuclear phenomena and/or about high-momentum components of the nuclear many-body wave function that arise from nucleon-nucleon correlations. Especially K^+-mesons have been considered as promising hadronic probes [19,20] due to the rather moderate final-state interaction, which is a consequence of strangeness conservation and the fact that there are no baryon resonances with antistrange quarks in nuclei. Antihyperons, furthermore, have a much larger production threshold and annihilate very fast in nuclei. On the other hand, the kaon properties might change in the nuclear medium [21] such that conclusions on cooperative nuclear phenomena require a precise understanding of the (anti) kaon potentials at finite nuclear density.

Experiments on $K^\pm$ production from nucleus-nucleus collisions at SIS energies of 1–2 A · GeV have shown that in-medium properties of the kaons are seen in the collective flow pattern of K^+-mesons both, in-plane and out of plane, as well as in the abundancy of antikaons [22,23]. Thus in-medium modifications of the mesons have become a topic of substantial interest in the last decade triggered in part by the early suggestion of Brown and Rho [24] that the modifications of hadron masses should scale with the scalar quark condensate $\langle q\bar{q}\rangle$ at finite baryon density.

As demonstrated in the pioneering work of Kaplan and Nelson [21] kaons and antikaons couple attractively to the scalar nucleon density with a strength proportional to the KN-Σ constant,

$$\Sigma_{KN} = \frac{1}{2}\big(m_u^0 + m_s^0\big)\langle N|\bar{u}u + \bar{s}s|N\rangle, \qquad (1)$$

[a] e-mail: Wolfgang.Cassing@theo.physik.uni-giessen.de

which is not well known at present and may vary from 270 to 450 MeV. In (1) m_u^0 and m_s^0 denote the bare masses for the light u- and strange s-quark while the expression in the brackets is the expectation value of the scalar light and strange quark condensate for the nucleon [22]. Furthermore, a vector coupling to the quark 4-current —for vanishing spatial components— leads to a repulsive potential term for the kaons; on the other hand, this (Weinberg-Tomozawa) term is attractive for the antikaons.

In chiral effective theories the dispersion relation for kaons and antikaons in the nuclear medium —for low momenta— can be written as [25]

$$\omega_K(\rho_N, \mathbf{p}) = +\frac{3}{8}\frac{\rho_N}{f_\pi^2} + \left[\mathbf{p}^2 + m_K^2\left(1 - \frac{\Sigma_{KN}}{f_\pi^2 m_K^2}\rho_s + \left(\frac{3\rho_N}{8 f_\pi^2 m_K}\right)^2\right)\right]^{1/2}, \quad (2)$$

$$\omega_{\bar{K}}(\rho_N, \mathbf{p}) = -\frac{3}{8}\frac{\rho_N}{f_\pi^2} + \left[\mathbf{p}^2 + m_K^2\left(1 - \frac{\Sigma_{KN}}{f_\pi^2 m_K^2}\rho_s + \left(\frac{3\rho_N}{8 f_\pi^2 m_K}\right)^2\right)\right]^{1/2}. \quad (3)$$

In eqs. (2), (3) m_K denotes the bare kaon mass, $f_\pi \approx 93$ MeV is the pion decay constant, while ρ_s and ρ_N stand for the scalar and vector nucleon densities, respectively. As shown in ref. [26], for $\Sigma_{KN} = 450$ MeV one ends up with an effective kaon potential which is close to zero below ordinary nuclear-matter density ρ_0 and becomes more repulsive above ρ_0. On the other hand, using $\Sigma_{KN} = 270$ MeV a repulsive kaon potential of ≈ 25 MeV at normal nuclear-matter density is obtained. Note that, when extrapolating (3) to $3\rho_0$ and above, the antikaon mass becomes very light. Thus antikaon condensates might occur at high baryon density which, furthermore, are of great interest in the astrophysical context [27–29].

However, the actual kaon and antikaon self-energies (or potentials) are quite a matter of debate —due to higher-order terms in the chiral expansion— especially for the antikaon [30–32] and the momentum dependence of their self-energies is widely unknown (except for a dispersion analysis in ref. [33]), since most Lagrangian models restrict to s-wave interactions or only include additional p-waves. It is thus mandatory to perform experimental studies of the (anti) kaon properties under well-controlled conditions, *e.g.* in proton-nucleus reactions, where one probes the (anti) kaon self-energies at normal nuclear-matter density $\rho_0 \approx 0.16\,\mathrm{fm}^{-3}$ and below. Furthermore, by gating on kaon momenta in the laboratory, one might be able to obtain information on the momentum dependence of the self-energies, too.

K^+ production in $p+A$ collisions at subthreshold energies has been observed experimentally more than a decade ago by Koptev *et al.* [20] at bombarding energies from 0.8 to 1.0 GeV. However, only total K^+ yields could be extracted at that time. Nevertheless, the target-mass dependence of the K^+ yield ($\sim A$) suggested the dominance of two-step reactions with an intermediate pion or Δ. Detailed folding-model calculations in refs. [17,18] essentially came to the same conclusion. First differential K^+ spectra from p + NaF and p + Pb reactions from the LBL Berkeley had been performed at $T_{\mathrm{lab}} = 2.1$ GeV [34], *i.e.* far above the NN threshold of 1.58 GeV in free space. Only in more recent years differential K^+ spectra have been measured down to 1.2 GeV for ^{12}C targets at 40° [35] (at SATURNE) or 90° in the laboratory [36] (at CELSIUS). Unfortunately, the different experiments have no overlap in acceptance and the interpretation of the data, if compatible at all, remains vague [15]. First data on the full momentum distribution at forward angles have been presented very recently by the ANKE Collaboration at COSY-Jülich [37] for K^+-mesons from p + ^{12}C reactions at 1.0 GeV [38]. These data show a kinematical focussing of the spectra at a finite momentum of $\approx 350\,\mathrm{MeV}/c$, which appears incompatible with the cross-section from ref. [36]. Thus, a systematic comparison of all data is urgently needed within an adequate theoretical approach that allows to compare the kinematically restricted data on the same footing.

In this study we use the coupled-channel (CBUU)[1] transport model that has first been developed in ref. [39] for the description of nucleus-nucleus collisions and later on employed for the simulation of pion- and proton-nucleus reactions [33,40,41] too. For applications to $K^\pm$ production in nucleus-nucleus collisions at SIS energies we refer the reader to ref. [42]. In this model the effects of momentum-dependent self-energies for all hadrons can be studied explicitly as well as their production and propagation in the nuclear medium.

The paper is organized as follows: We briefly recapitulate the ingredients of the CBUU model in sect. 2, present the extensions performed in this study with respect to the treatment of K^+Y differential production channels from secondary πN reactions and investigate in particular the effects from K^+N rescattering. In sect. 3 we compare the transport calculations to the experimental spectra available from different laboratories and explore the sensitivity of the K^+ spectra to the momentum-dependent potentials employed. A summary and discussion of open problems concludes this paper in sect. 4.

2 Ingredients of the extended transport model

In this work we perform our analysis along the line of the CBUU approach [39] which is based on a coupled set of transport equations for the phase-space distributions

[1] Coupled-Channel Boltzmann-Uehling-Uhlenbeck.

$f_h(x,p)$ of hadron h, *i.e.* [43,44]

$$\begin{aligned}&\big(\Pi_\mu - \Pi_\nu \partial_\mu^p U_h^\nu - M_h^* \partial_\mu^p U_h^S\big)\partial_x^\mu f_h(x,p) \qquad (4)\\ &+\big(\Pi_\nu \partial_\mu^x U_h^\nu + M_h^* \partial_\mu^x U_h^S\big)\partial_p^\mu f_h(x,p) = \\ &\sum_{h_2 h_3 h_4 \ldots} \int \mathrm{d}2\,\mathrm{d}3\,\mathrm{d}4 \ldots [G^\dagger G]_{12\to 34\ldots} \\ &\times \delta^4(\Pi + \Pi_2 - \Pi_3 - \Pi_4 \cdots) \\ &\times \big\{ f_{h_3}(x,p_3) f_{h_4}(x,p_4) \bar{f}_h(x,p) \bar{f}_{h_2}(x,p_2) \\ &- f_h(x,p) f_{h_2}(x,p_2) \bar{f}_{h_3}(x,p_3) \bar{f}_{h_4}(x,p_4) \big\} \ldots . \qquad (5)\end{aligned}$$

In eq. (4) $U_h^S(x,p)$ and $U_h^\mu(x,p)$ denote the real part of the scalar and vector hadron self-energies, respectively, while $[G^\dagger G]_{12\to 34\ldots}\delta^4(\Pi + \Pi_2 - \Pi_3 - \Pi_4 \cdots)$ is the "transition rate" for the process $1+2 \to 3+4+\cdots$ which is taken to be on-shell in the semiclassical limit adopted. The hadron quasi-particle properties in (4) are defined via the mass-shell constraint

$$\delta(\Pi_\mu \Pi^\mu - M_h^{*2}), \qquad (6)$$

with effective masses and momenta (in local Thomas-Fermi approximation) given by [43]

$$\begin{aligned}M_h^*(x,p) &= M_h + U_h^S(x,p),\\ \Pi^\mu(x,p) &= p^\mu - U_h^\mu(x,p),\end{aligned} \qquad (7)$$

while the phase-space factors

$$\bar{f}_h(x,p) = 1 \pm f_h(x,p) \qquad (8)$$

are responsible for fermion Pauli blocking or Bose enhancement, respectively, depending on the type of hadron in the final/initial channel. The dots in eq. (5) stand for further contributions to the collision term with more than two hadrons in the final/initial channels (cf. ref. [45]). The transport approach (4) is fully specified by $U_h^S(x,p)$ and $U_h^\mu(x,p)$ ($\mu = 0,1,2,3$), which determine the mean-field propagation of the hadrons, and by the transition rates $G^\dagger G\,\delta^4(\ldots)$ in the collision term (5), that describes the scattering and hadron production/absorption rates.

The scalar and vector mean fields U_h^S and U_h^μ for nucleons are modeled as in ref. [44], however, slightly modified in line with ref. [46]. In fig. 1 the real part of the nucleon potential $U_N(p)$, defined by the difference between the in-medium and vacuum energy

$$U_N(p) = \Pi^0(\mathbf{p}) - \sqrt{\mathbf{p}^2 + M_0^2}, \qquad (9)$$

where M_0 denotes the "free" nucleon mass, is shown at density ρ_0 (solid line) as a function of the momentum p relative to the nuclear matter at rest. Whereas we see a net attraction for momenta $p \leq 0.6\,\mathrm{GeV}/c$, the nucleon potential becomes repulsive for higher momenta and reaches a maximum repulsion at $p \approx 1.5\,\mathrm{GeV}/c$. We mention that at density ρ_0 the potential $U_N(p)$ (9) compares well with the potential from the data analysis of Hama *et al.* [47] as well as Dirac-Brueckner computations from [48] up to a kinetic energy E_{kin} of 1 GeV [44].

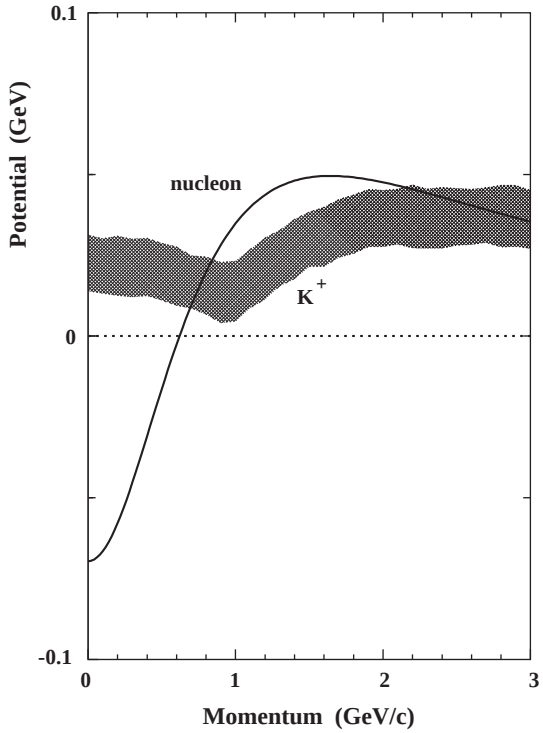

Fig. 1. The nucleon potential (9) (solid line) at density ρ_0 as a function of momentum relative to the nuclear matter at rest as used in the CBUU transport approach. The hatched area denotes the nuclear K^+ potential at density ρ_0 (within the uncertainties) from the dispersion analysis in ref. [33].

Apart from the nuclear potentials each charged hadron additionally moves in the background of the Coulomb potential that is generated by the charged hadrons themselves. In case of proton-nucleus reactions —with the nucleus at rest— this essentially amounts to a Coulomb acceleration in the final state for positively charged hadrons and a deceleration for negatively charged particles. Note that, for heavy nuclei like Pb or Au the Coulomb potential in the nuclear interior (for p, π^+, K^+) is $\sim 20\,\mathrm{MeV}$, *i.e.* of the same order of magnitude as the "expected" repulsive K^+ nuclear potential.

The hyperon mean fields, furthermore, are assumed to be 2/3 of the nucleon potentials. In the present approach, apart from nucleons, Δ, $N(1440)$, $N(1535)$, Λ, Σ with their isospin degrees of freedom, we propagate explicitly pions, K^+, K^-, and η's and assume that the pions as Goldstone bosons do not change their properties in the medium; we also discard self-energies for the η-mesons which have a minor effect on the kaon dynamics. The kaon and antikaon potentials, however, have to be specified explicitly.

2.1 K^+ and K^- self-energies

Apart from (2), (3) there is a couple of models for the kaon and antikaon self-energies [21,27,49], which differ in the actual magnitude, however, agree on the relative signs for

kaons and antikaons. Thus, in line with the kaon-nucleon scattering amplitude the K^+ potential should be slightly repulsive at finite baryon density, whereas the antikaon should see an attractive potential in the nuclear medium. Without going into a detailed discussion of the various models (cf. ref. [26] and figures therein) we adopt the more practical point of view, that the actual K^+ and K^- self-energies are unknown and as a guide for our analysis use a linear extrapolation of the form

$$m_K^*(\rho_B, p) = m_K^0 \left(1 + \alpha(p)\frac{\rho_B}{\rho_0}\right), \tag{10}$$

with $\alpha(p)$ denoting a momentum-dependent coefficient. Following the dispersion analysis of Sibirtsev *et al.* [33] the coefficients $\alpha(p)$ can be modelled in line with the $K^\pm$ potentials from fig. 9 of [33]; the resulting kaon potential U_{K^+} at density ρ_0 is shown in fig. 1 in terms of the hatched area and remains repulsive for all momenta considered. In the momentum range of interest in this study, *i.e.* 0.1–1.0 GeV/c, the K^+ potential at density ρ_0 may be approximately represented by a constant of $U_{K^+} \approx 20$ MeV taking into account the relative uncertainty of ± 10 MeV from the analysis in ref. [33]. Since the antikaon dynamics has been investigated in ref. [33] for $p + A$ reactions, we skip a further description of the actual implementation of the K^- potential.

2.2 Perturbative treatment of strangeness production

The calculation of "subthreshold" particle production has to be treated perturbatively in the energy regime of interest due to the small cross-sections involved. Since we work within the parallel ensemble algorithm in the CBUU approach, each parallel run of the transport calculation can be considered approximately as an individual reaction event, where binary reactions in the entrance channel at given invariant energy $\sqrt{s}$ lead to final states with 2 (*e.g.*, K^+Y in πB channels), 3 (*e.g.*, for K^+YN channels in BB collisions) or 4 particles (*e.g.*, $K\bar{K}NN$ in BB collisions) with a relative weight P_i for each event i which is defined by the ratio of the production cross-section to the total hadron-hadron cross-section[2]. We thus dynamically gate on all events where a K^+Y or K^+K^- pair is produced initially. Each strange hadron production event i is represented by $\sim 10^3$ test particles for the final strange hadron j with individual weight W_j^i such that the sum of the weights W_j^i over j reproduces the individual production probability P_i and the distribution in momenta (multiplied with the NN or πN cross-section) describes the differential production cross-section (see below).

We use two different strategies to simulate the momentum differential distribution of kaons and hyperons in NN or ΔN and πN collisions: For NN or ΔN reactions —in their center-of-mass system— we generate for each collision event, *e.g.* 10^3, final states of the type K^+YN by Monte Carlo according to 3-body phase (including the potential effects on their energies). The four-momenta k_i of the particles then are Lorentz-transformed to the calculational frame and the individual weights W_i^j ($j = 1, \ldots, 1000$) are determined from the ratio of the differential production cross-section (for the kaon momentum k_i) and the total pN or ΔN cross-section. When performing ~ 100 parallel runs and ~ 100 subsequent simulations this gives (*e.g.*, at $T_{\rm lab} = 2.3$ GeV) about 10^7 kaons and hyperons with individual weights. This number of strange hadrons is sufficient to represent their Lorentz-invariant differential momentum distribution with good statistics. Note that, a high statistics is mandatory for the K^+ spectra especially when restricting to narrow angular bins in the laboratory.

The above recipe is traditionally employed in transport simulations of nucleus-nucleus reactions [42]. However, in case of secondary $\pi N \to KY$ reactions the Monte Carlo simulation described above does not give sufficient statistics for momentum differential spectra from πN collisions in case of $p + A$ reactions. This is due to the fact that the pion multiplicity per reaction is typically lower than 1 and only a small fraction of the energetic pions (*e.g.*, at $T_{\rm lab} = 1$ GeV) can lead to a K^+Y final state. On the other hand, the secondary πN reactions are expected [17] to give the dominant contribution to K^+ production at subthreshold bombarding energies. In order to resolve this "technical" problem, we go back to an integral formulation for differential kaon yields from πN collisions (cf. subsect. 2.5) and calculate the corresponding integrals numerically on a fixed grid in three-momentum $\mathbf{k}$. Each grid point then is represented by a kaon test particle with 3-momentum $\mathbf{k}$ and a weight determined from (17), while the quasiparticle energy E_K includes the local potential energy.

Once produced the "perturbative" hadrons are propagated according to the Hamilton equations of motion including the potentials. Elastic and inelastic reactions with pions, η's or nonstrange baryons are computed in the standard way [39]. The final differential cross-sections are obtained by multiplying each test particle weight W_j^i by the total inelastic pA cross-section and gating on the experimental acceptance of the different detectors[3]. In this way one achieves a realistic simulation of the strangeness production, propagation and reabsorption during the proton-nucleus collision with sufficient statistics to allow for selective cuts also at the low bombarding energy of 1.0 GeV, where the total K^+ cross-section is in the order of 1 μb (for Au) or below (for ^{12}C).

2.3 Elementary cross-sections

For the present study the production of pions by pN collisions in $p + A$ reactions as well the total kaon cross-sections in pN and πN collisions are of relevance. The pion production cross-section from NN interactions is based on the parametrization of the experimental data by

[2] The actual final states are chosen according to the 2-, 3-, or 4-body phase space.

[3] The cross-sections are normalized by default to the number of parallel runs and subsequent simulations.

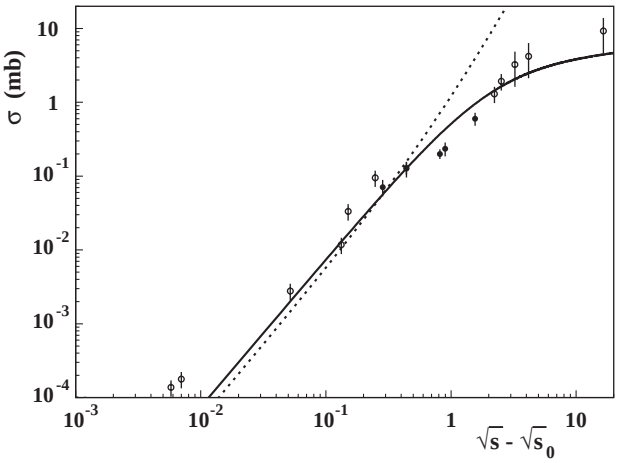

Fig. 2. Comparison of our parametrization for the inclusive K^+ production cross-section in pp reactions (solid line) with the data from refs. [52,53]. The dotted line corresponds to the parametrization from Zwermann [54] used earlier in refs. [17, 18].

Ver West and Arndt [50] and implemented in the transport model as described in ref. [39]. The cross-sections for the channels $\pi N \to KY$, where Y stands for a hyperon Λ, Σ, are taken from the analysis of Huang *et al.* [51] and essentially correspond to the experimental data for the different πN channels in vacuum (or "free" space). Note that, in addition to our early studies in [17,18] the channels with a Σ-hyperon are taken into account. All cross-sections are reparametrized as a function of the invariant energy above threshold $\sqrt{s} - \sqrt{s_0}$ [22], where $\sqrt{s_0}$ denotes the threshold for the individual channel given by the sum of the hadron masses in the final state of the reaction. We recall that the differential cross-sections for binary reactions are fully determined by the total cross-sections when assuming an S-wave dominance.

Whereas the production cross-section of kaons from pN collisions close to threshold has been essentially unknown about a decade ago, the ambiguity in this cross-section has been resolved experimentally by now [52] and more adequate parametrizations of the cross-sections can be employed. The experimental data from refs. [52,53] on the $pp \to K^+ + X$ reactions are displayed in fig. 2 in comparison to the current approximation (solid line) and the estimate from Zwermann [54] (dotted line) used earlier [17, 18]. Thus the problem of "free" cross-sections for pN collisions is sufficiently under control. For ΔN collisions, however, no experimental data are available. We use the same cross-section as a function of the invariant energy $\sqrt{s}$ as in the pN case keeping in mind this basic uncertainty.

The question arises, furthermore, about the in-medium production cross-sections —essentially at density ρ_0— if potentials or self-energies are involved. Here we employ the assumption that the production matrix element squared $|M|^2$ does not change in the medium and the change of cross-section can be described by a change of the available phase space. This notion is guided by the experimental observation that meson production from pp collisions is well described by phase space [55,56] if final-state interactions (FSI) between the hadrons are taken into account. These FSI, furthermore, are found to be dominated by the final baryon-baryon interaction, which is very strong in the pp, pn or $p\Lambda$ channels in free space. On the other hand, such FSI are screened in the nuclear medium due to the surrounding nucleons such that in-medium production cross-sections for mesons are expected to vary essentially with the available phase space. It is thus sufficient to shift the threshold in a pN collision to

$$\sqrt{s_0^*} = \Pi_N^0(p_N) + \Pi_\Lambda^0(p_\Lambda) + \Pi_K^0(p_K) \qquad (11)$$

using (7), where the momenta p_N, p_Λ, p_K denote the relative momenta with respect to the nuclear-matter rest frame.

2.4 Folding model and its limitations

We briefly recall the assumptions of the folding model, that is used in part for the evaluation of momentum-dependent differential production probabilities from secondary pion-nucleon collisions in the CBUU approach (cf. subsect. 2.5). It is described in more detail for proton-nucleus reactions in [17,57,58]. The underlying picture is that the proton impinging on a nucleus at a bombarding energy $T_{\rm lab} > 400\,\mathrm{MeV}$ is producing a meson x with momentum k_x only in the first collision due to the available energy in the reaction. The Lorentz-invariant differential cross-section to produce a meson in a primary proton-nucleon (pN) collision is given by [57]

$$\left(E_x \frac{\mathrm{d}^3\sigma_x^{NN}}{\mathrm{d}^3 k_x}\right)_{\rm prim.} = \int \mathrm{d}^3p\,\mathrm{d}\omega \left(E_x' \frac{\mathrm{d}^3\sigma_x^e(\sqrt{s})}{\mathrm{d}^3 k_x'}\right) S(\mathbf{p},\omega), \qquad (12)$$

where the Pauli-blocking factor for the final nucleon states is neglected since kinematically the nucleons end up in an unoccupied regime in momentum space at the bombarding energies of interest. In eq. (12) $S(\mathbf{p},\omega)$ stands for the target spectral function (normalized to 1) which can be taken from experiment, *e.g.* ref. [59], or parametrized accordingly. In eq. (12) the primed indices denote meson momenta in the individual nucleon-nucleon cms frame which have to be Lorentz transformed to the detection frame. The quantity $\sqrt{s}$ is the invariant energy of the individual NN system, while the elementary differential cross-section $\mathrm{d}^3\sigma_x^e(\sqrt{s})/\mathrm{d}^3k_x$ in (12) is parametrized according to phase space (cf. [17]) and assumed to be isotropic in the NN cms frame.

In order to obtain the inclusive differential kaon cross-section in a $p + A$ reaction within the folding model, one has to multiply the differential cross-section (12) by the number of first-chance collisions $N_1(A)$. This number is approximately given by the area of the target divided by the pN cross-section, *i.e.* $N_1(A) \approx \pi R_{\rm target}^2/\sigma_{pN}$. To be more accurate one can use Glauber theory which leads to $N_1 \approx 7.3$ for $p + {}^{12}\mathrm{C}$ [18,35]. The contributions to the K^+ yield from secondary or further sequential NN collisions

is discarded in the folding model at subthreshold energies due to the energy straggling of the impinging proton and due to the fact that already the first-chance collisions only give a minor contribution to the K^+ yield observed experimentally.

Apart from the primary reaction channels described above, the first NN collision may also lead to the excitation of a Δ-resonance or even higher baryon resonances (*e.g.*, $N(1440), N(1535), \ldots$) which decay to nucleons and essentially pions due to their short lifetimes of $\approx 1\,\mathrm{fm}/c$ or collide with another nucleon before decaying. The differential cross-section to produce a K^+-meson in a collision of an on-shell pion with a nucleon from the target at invariant energy $\sqrt{s}$ then is given by

$$\left(E_K \frac{\mathrm{d}^3\sigma_K^{\pi N}}{\mathrm{d}^3k}\right) = \sum_c \int \mathrm{d}^3p\,\mathrm{d}\omega S(\mathbf{p},\omega) \times \left(E'_K \frac{\mathrm{d}^3\sigma_{\pi N\to YK^+}(\sqrt{s})}{\mathrm{d}^3k'}\right)_c \quad (13)$$

similar to (12), where now the differential cross-sections for the reactions $\pi N \to K^+Y$ enter. Here, the index c denotes all individual channels while the hyperon Y stands again for a Λ- or Σ-baryon.

In order to evaluate the K^+ yield from secondary $\pi N \to K^+Y$ collisions, one folds the primary pion distribution —given by the primary differential pion cross-section that is divided by the total pN cross-section σ_{tot}— with the nucleon spectral function $S(\mathbf{p},\omega)$ and the invariant production cross-section, *i.e.*

$$\left(E_K \frac{\mathrm{d}^3\sigma_K}{\mathrm{d}^3k}\right)_{\mathrm{sec.}} = \sum_c \int\int \frac{\mathrm{d}^3p\,\mathrm{d}\omega}{\sigma_{\mathrm{tot}}} \frac{\mathrm{d}^3k'_\pi}{E'_\pi} S(\mathbf{p},\omega) \times \left(E'_K \frac{\mathrm{d}^3\sigma_{\pi N\to YK^+}(\mathbf{p},\mathbf{k}'_\pi)}{\mathrm{d}^3k'}\right)_c \left(E'_\pi \frac{\mathrm{d}^3\sigma_{pN\to\pi X}}{\mathrm{d}^3k'_\pi}\right)_{\mathrm{prim.}} \times g_\pi(A). \quad (14)$$

In eq. (14) the single prime indices denote the system of the intermediate pion and a target nucleon. Moreover, $E'_\pi \mathrm{d}^3\sigma_{pN\to\pi X}/\mathrm{d}^3k'_\pi$ stands for the π-meson differential cross-section, which is calculated according to (12), while σ_{tot} denotes the total proton-nucleon cross-section. The factor $g_\pi(A)$ in (14) accounts for the probability that the pion interacts again with a target nucleon (cf. [57]). Note that, by eq. (14) the intermediate pion is assumed to be on-shell which might not hold for deep subthreshold kaon production. As in case of the primary channel the expression (14) has to be multiplied by $N_1(A)$ in the folding model. Furthermore, some estimate for the secondary rescattering probability $g_\pi(A)$ has to be employed as, *e.g.*, described in ref. [60].

The one- and two-step folding model has been used often in the analysis of kaon- or η-meson production [17, 18,35,57,58,61,62] initially employing parametrized momentum distributions (cf. refs. [17,18]) instead of spectral functions. They allow for an estimate of differential cross-sections in case of weakly interacting probes and may serve as reference calculations for more involved simulations employing all initial- and final-state interactions during the reaction as the transport approach developed here.

2.5 Implementation of K^+ production from πN collisions

Whereas kaon production from pN, ΔN or resonance-nucleon reactions is treated in the CBUU approach dynamically as described in subsect. 2.2, a different implementation is used for πN collisions. This is necessary since energetic secondary pion-nucleon collisions suffer from very low statistics in transport simulations of $p + A$ reactions. On the other hand, their contribution to the kaon yield is expected to be high at subthreshold energies [17, 18]. We thus implement the secondary pion-nucleon production channels for kaons following concepts of the folding model as described below.

We note that the primary differential multiplicity of pions (with charge $Z = -1, 0, 1$), *i.e.*

$$\left(E_\pi \frac{\mathrm{d}^3M_\pi}{\mathrm{d}^3k_\pi}\right)^Z \quad (15)$$

can be calculated in the transport model directly, however, with low statistics in the high-momentum tails. In (15) we address to the pion spectrum before rescattering with a nucleon which has to be distinguished from the final pion spectrum for $t \to \infty$. An integration of (15) with respect to d^3k_π/E_π gives the primary multiplicity of pions with charge Z, while dividing (15) by this number we obtain the normalized primary pion spectrum from the transport calculation. On the other hand, the primary differential pion spectrum from the folding model can be evaluated from

$$\left(E_\pi \frac{\mathrm{d}^3M_\pi}{\mathrm{d}^3k_\pi}\right)^Z_{\mathrm{prim.}} = \frac{1}{N_Z} \int \frac{\mathrm{d}^3p\,\mathrm{d}\omega}{\sigma_{\mathrm{tot}}} S(\mathbf{p},\omega) \times \left(E'_\pi \frac{\mathrm{d}^3\sigma_{pN\to\pi+X}(\sqrt{s})}{\mathrm{d}^3k'_\pi}\right)^Z, \quad (16)$$

where the factor N_Z ensures a normalization to unity. In fact, the distributions (15) and (16) turn out to be identical —within statistics due to the Monte Carlo simulation for the pion spectrum in the transport approach— since the same differential pion production cross-sections are used. The only remarkable difference lies in the high-momentum tails, which (in contrast to (15)) are given by (16) with good accuracy.

The differential probability, to produce a K^+ with momentum $\mathbf{k}$, *e.g.*, in the reaction $\pi^0 p \to K^+\Lambda$ then is given by folding the pion distribution function (16) with the corresponding production cross-section and the nucleon spectral function

$$\left(E_K \frac{\mathrm{d}^3P_{K^+}}{\mathrm{d}^3k}\right) = \int\int \frac{\mathrm{d}^3p\,\mathrm{d}\omega}{\sigma_{\pi N}} \frac{\mathrm{d}^3k'_\pi}{E'_\pi} S(\mathbf{p},\omega) \times \left(E'_K \frac{\mathrm{d}^3\sigma_{\pi^0 p\to K^+\Lambda}(\sqrt{s})}{\mathrm{d}^3k'}\right) \left(E'_\pi \frac{\mathrm{d}^3M_\pi}{\mathrm{d}^3k'_\pi}\right)^{Z=0}_{\mathrm{prim.}}. \quad (17)$$

Similar equations hold for the channels $\pi^0 p \to K^+\Sigma^0$, $\pi^- p \to K^+\Sigma^-$, $\pi^+ p \to K^+\Sigma^+$, that are calculated separately and implemented in the transport approach for each primary πN collisions. Roughly speaking, in the transport calculation the number of primary πN reactions is calculated dynamically for all secondary channels c —for each system A and energy $T_{\rm lab}$— and the differential K^+ multiplicity is obtained by multiplying these dynamical numbers with the differential probabilities (17) and summing up all channels c.

We point out, that the implementation described above compares well with the Monte Carlo scheme (subsect. 2.2) for secondary πN reactions concerning the total number of kaons produced from $T_{\rm lab} = 1.5$–$2.3\,\mathrm{GeV}$, while the details in the differential spectra cannot be controlled at low $T_{\rm lab}$ by the Monte Carlo simulations due to low statistics as mentioned before. Thus, it is very difficult to give an estimate for a "systematic error" with respect to the implementation used. Only a detailed comparison to data —preferentially taken by the same collaboration— for different target nuclei from $\sim 1\,\mathrm{GeV}$ to laboratory energies above $K^+\Lambda$ threshold will finally shed some light on the "errors" involved.

2.6 K^+ rescattering

As indicated in subsect. 2.4, the folding model is useful for the evaluation of total K^+ yields, however, becomes questionable in case of differential spectra especially for heavy targets like Au or Pb, since kaon elastic rescattering cannot be described in a straightforward manner. In order to show the influence of K^+ rescattering on the kaon spectra at different angles we show in fig. 3 a comparison of our extended CBUU calculations with (solid lines) and without (dashed lines) kaon rescattering for p + Pb at $1.5\,\mathrm{GeV}$. As can be seen from fig. 3 the K^+ yield in forward direction ($\theta \leq 15^\circ$) is reduced by up to a factor of 2, while for large angles in the laboratory (80°) the kaon spectra become enhanced and also shifted to lower momenta in the laboratory. Thus, rescattering has to be included as a necessary ingredient for the calculations if comparisons to differential spectra are made on an absolute scale and especially, if one attempts to extract kaon potentials from the spectral shape (see below). We note that kaon rescattering thus will always be included in the calculations to be shown in the following. Furthermore, we mention that the results from the folding model (12), (14) agree with the resulting spectra from the CBUU calculation for p + Pb and p + C at $1.5\,\mathrm{GeV}$ within 30% when neglecting final-state interactions as well as nuclear and Coulomb potentials.

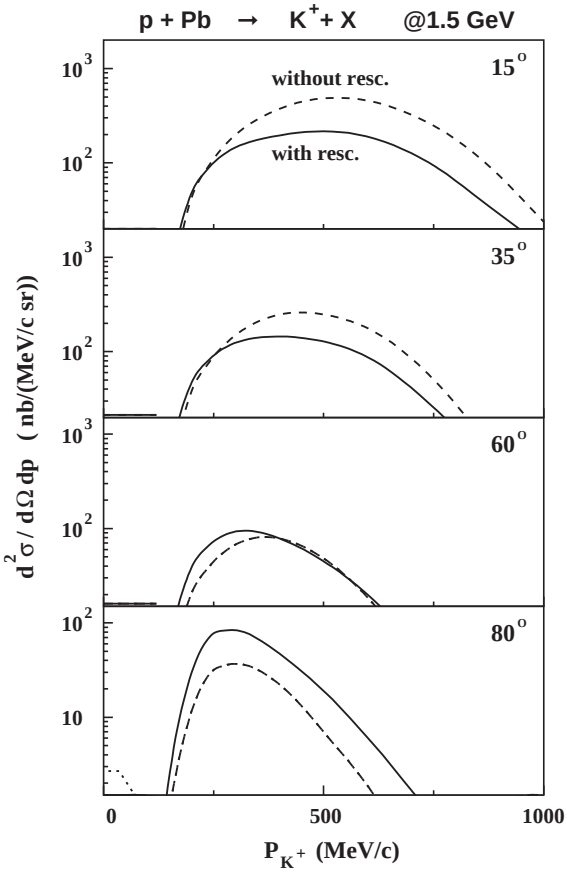

Fig. 3. Comparison of the differential K^+ spectra for p + Pb at $1.5\,\mathrm{GeV}$ at different angles in the laboratory from 15° to 80°. The solid lines are obtained from CBUU calculations including kaon rescattering, whereas the dashed lines are without rescattering.

3 Comparison to experimental data

In this section we compare our calculations to the experimental K^+ spectra available from $1.0\,\mathrm{GeV}$ to $2.5\,\mathrm{GeV}$ bombarding energy on different targets. In order to have an identical assignment of lines in this section the dotted lines in figs. 4-9 correspond to CBUU calculations without baryon and kaon potentials, the dashed lines show the results with baryon potentials included while the solid lines reflect calculations including both, nucleon and kaon potentials as specified in fig. 1. In all calculations, furthermore, the Coulomb potential will be included by default.

We start in fig. 4 with a comparison to the data of the KaoS/SPES3 Collaboration for the differential K^+ spectra for p + Pb and p + C at $1.5\,\mathrm{GeV}$ and $\theta_{\rm lab} = 40 \pm 5^\circ$ from SATURNE [35]. The experimental spectra for the Pb target are seen to be described roughly within the error bars for all calculations, *i.e.* with and without potentials, such that one is not very sensitive to in-medium potentials at $1.5\,\mathrm{GeV}$ in the momentum range above $350\,\mathrm{MeV}/c$. For lower kaon momenta the repulsive K^+ potential leads to a sizeable decrease (or shift) in the spectra which can be attributed to the additional acceleration of the kaons by the nuclear K^+ potential when propagating from the nuclear interior to the vacuum. In case of the ^{12}C target the effects from the momentum-dependent nucleon potentials as well as from the K^+ potential are similar to the Pb target. It both cases the calculations without potentials

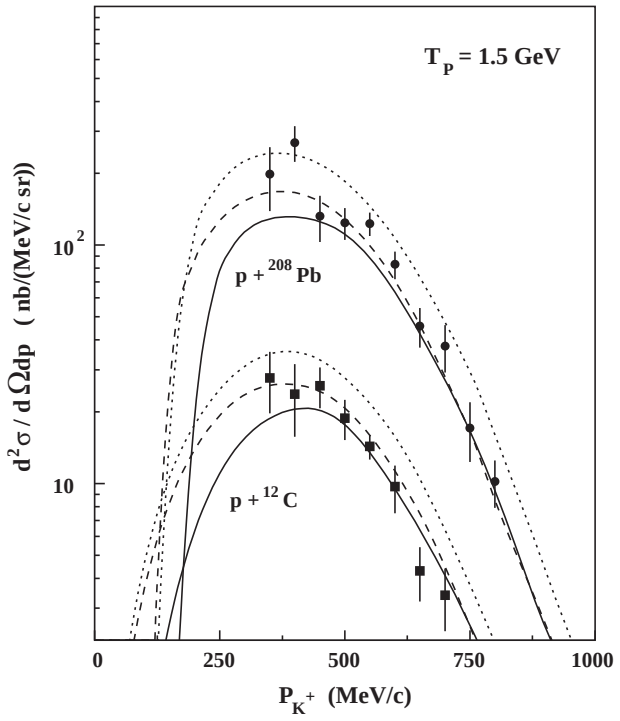

Fig. 4. Comparison of the CBUU calculations for the differential K^+ spectra for p + Pb and p + C at 1.5 GeV and $\theta_{\rm lab} = 40 \pm 5°$ with the experimental data from ref. [35]. The dotted lines are obtained from CBUU calculations without baryon and kaon potentials, the dashed lines show the results with baryon potentials included, while the solid lines correspond to calculations including both nucleon and kaon potentials. Note that, the effect of the repulsive kaon potential is a reduction of the total K^+ yield as well as a shift of the spectra at lower momenta.

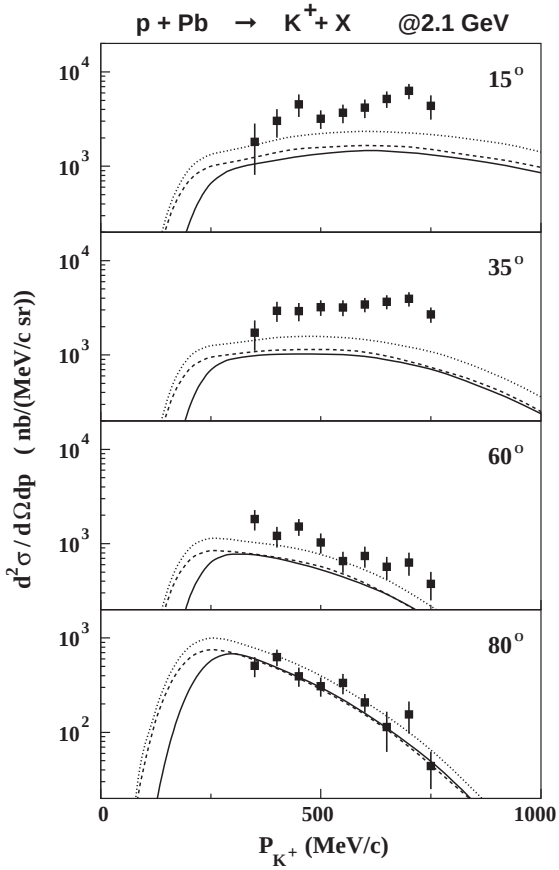

Fig. 5. Comparison of the CBUU calculations for the differential K^+ spectra for p + Pb at 2.1 GeV with the experimental data from ref. [34] at different angles in the laboratory. The dotted lines are obtained from CBUU calculations without baryon and kaon potentials, the dashed lines show the results with baryon potentials included, while the solid lines correspond to calculations including both nucleon and kaon potentials.

(dotted lines) slightly overestimate the data, but it is not possible to draw already some conclusion on the actual size of the K^+ potential since a single comparison might suffer from systematic errors.

In figs. 5 and 6 we compare the CBUU calculations for the differential K^+ spectra for p + Pb and p + NaF at 2.1 GeV with the experimental data from the LBL Berkeley [34] for different laboratory angles from 15° to 80°. At this bombarding energy the nucleon and Λ final momenta on average are above 0.6 GeV/c such that their potentials at finite density (cf. fig. 1) are repulsive. As a consequence the calculated kaon yield decreases when including the baryon potentials in the final state. Taking into account additionally the repulsive K^+ potential decreases essentially the spectrum for momenta below 250 MeV/c, but leaves the spectrum practically unmodified for higher momenta, since the relative change of the K^+ energy by the kaon potential is only small.

In all approximations the experimental spectra are underestimated by factors $\sim$ 2–3 at 15° and 35°, which at first sight might be attributed to an improper energy dependence of the calculations. However, a comparison of the CBUU calculations for p + Au with the preliminary data from ref. [63] (taken at GSI) and p + C at 2.5 GeV and $\theta_{\rm lab} = 40 \pm 5°$ with the experimental data from SATURNE [35] in fig. 7 shows that these spectra are overestimated by up to a factor of 2–3 at higher kaon momenta. Note that, the corresponding data from ref. [63] so far have to be considered as preliminary. These findings suggest that the spectra from ref. [34] are systematically too high by about factors of 2–3 or the data from the KaoS Collaboration too low (by about the same factor).

To further test the (over) underprediction of the transport model we show in fig. 8 a comparison of the CBUU calculations for the differential K^+ spectra for p + C at 1.2 GeV with the experimental data from ref. [36] at $\theta_{\rm lab} = 90°$ (open circles) taken at CELSIUS and $\theta_{\rm lab} = 40 \pm 5°$ (full squares) from the KaoS/SPES3 Collaboration [35] taken at SATURNE. In this particular case the spectra from ref. [35] are slightly overestimated by the calculations when neglecting the kaon potential while the spectra from ref. [36] at 90° are underestimated by about a factor of 5–6 when neglecting the repulsive K^+ potential and by about an order of magnitude for the repulsive kaon potential included, which leads again to a sizeable decrease

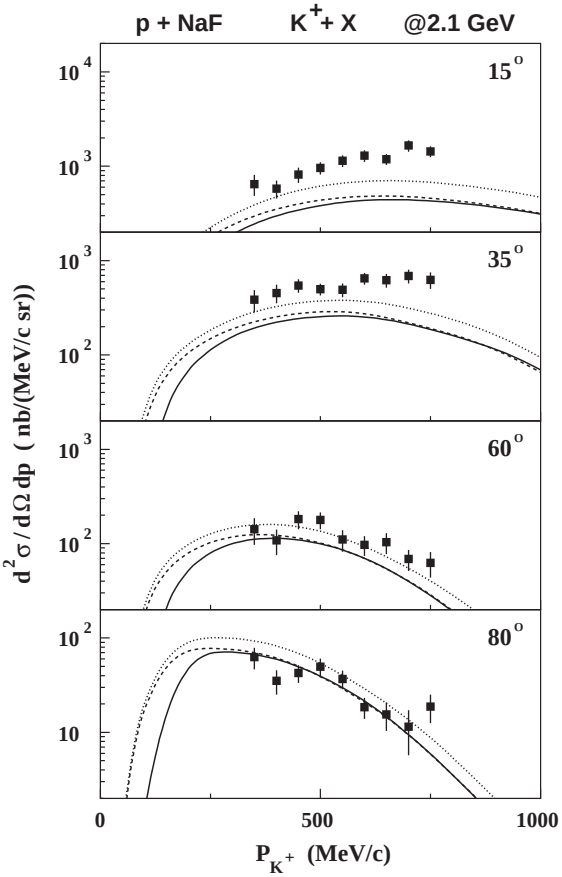

Fig. 6. Comparison of the CBUU calculations for the differential K^+ spectra for p + NaF at 2.1 GeV with the experimental data from ref. [34] at different angles in the laboratory. The dotted lines are obtained from CBUU calculations without baryon and kaon potentials, the dashed lines show the results with baryon potentials included, while the solid lines correspond to calculations including both nucleon and kaon potentials.

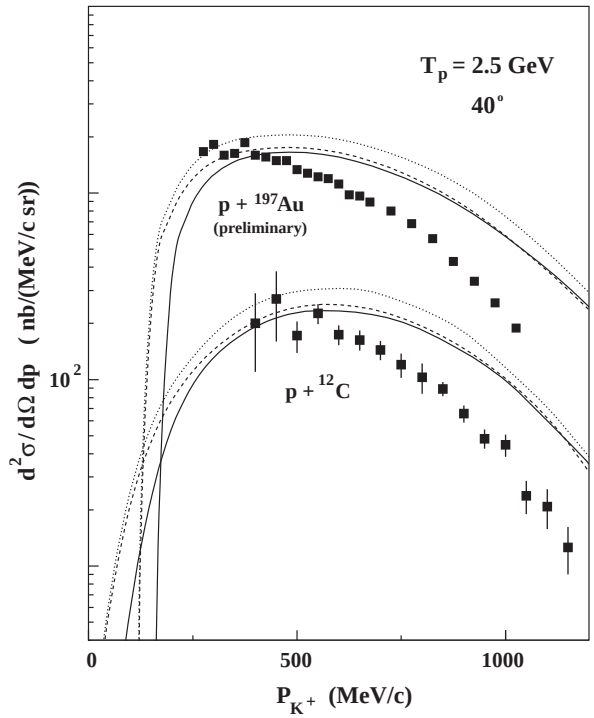

Fig. 7. Comparison of the CBUU calculations for the differential K^+ spectra for p + Au (upper part) and p + C (lower part) at 2.5 GeV and $\theta_{\rm lab} = 40 \pm 5°$ with the experimental data from refs. [63,35]. The dotted lines are obtained from CBUU calculations without baryon and kaon potentials, the dashed lines show the results with baryon potentials included, while the solid lines correspond to calculations including both nucleon and kaon potentials.

of the spectra at low momentum. It is not clear to the authors where such discrepancies might come from.

The CBUU calculations demonstrate that the kaon spectra at 90° and 40° are slightly enhanced (dashed lines) when taking the nucleon potential effects into account. Contrary to the kinematical situation at $T_{\rm lab} = 2.1$ (or 1.5) GeV the nucleon and Λ final momenta here on average are below 0.6 GeV/c, where the potentials are attractive (cf. fig. 1), such that the K^+ production becomes enhanced (dashed lines) relative to the free case (dotted lines). When including additionally the overall repulsive kaon potential the K^+ spectrum drops again (solid lines).

We now turn to the kinematical conditions of the ANKE experiments at COSY-Jülich [37], that have taken K^+ spectra in forward direction for $\theta_{\rm lab} \leq 12°$. The calculated differential K^+ spectra for p + ^{12}C at 1.0 GeV for $\theta_{\rm lab} \leq 12°$ are displayed in fig. 9 in comparison to the data from ref. [38]. The dotted lines again are obtained from CBUU calculations without baryon and kaon potentials, the dashed lines show the results with baryon potentials included while the solid lines correspond to calculations with both, nucleon and kaon potentials. At this low bombarding energy the net attractive baryon potentials in the final state enhance the K^+ yield by about a factor of 2 whereas the additional repulsive K^+ potential leads again to a decrease by a factor ~ 3. The data from ref. [38] are rather well described by the calculations that include the baryon and K^+ potentials (solid line), whereas the other limits clearly fail. This might be considered as a first indication for the observation of a repulsive K^+ potential in $p+A$ reactions, however, a full systematics in target mass A and laboratory energy $T_{\rm lab}$ will be needed to pin down this effect unambiguously.

Without explicit representation we mention that at $T_{\rm lab} = 1.0$ GeV the contributions from the two-step mechanisms $\Delta N \to K^+YN$ and $\pi N \to K^+Y$ amount to $\sim$ 75% for a ^{12}C target and to $\sim$ 90% for an Au target. Thus, the dominant fraction of the K^+ yield is due to the secondary channels in line with the earlier calculations in refs. [17,18]. Consequently, one does not probe high-momentum components of the nuclear wave function by K^+ spectra at subthreshold energies in a direct way. At $T_{\rm lab} = 2.3$ GeV the secondary channels in case of an Au target amount to about 30% and in case of a C target to less than 20%. This relative change with target mass number is attributed to the fact that for the small ^{12}C

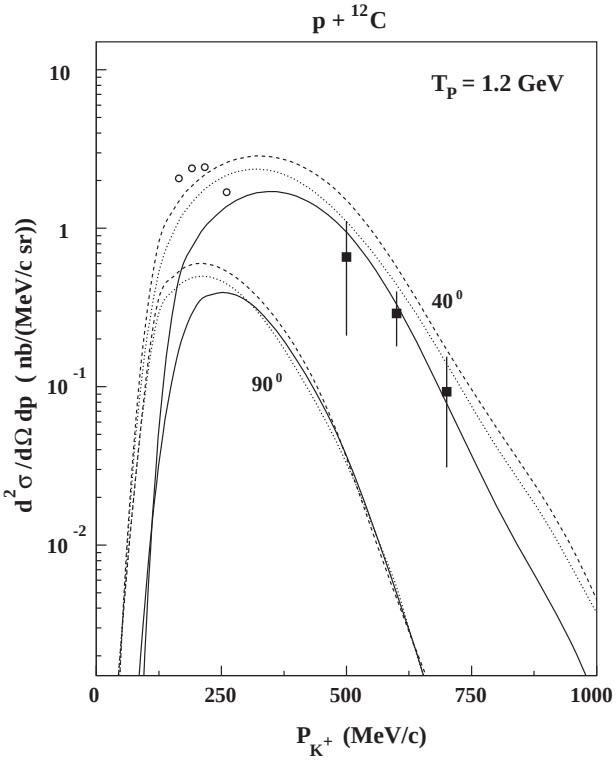

Fig. 8. Comparison of the CBUU calculations for the differential K^+ spectra for p + C 1.2 GeV with the experimental data from ref. [36] at $\theta_{\rm lab} = 90^\circ$ (open circles; lower lines) and $\theta_{\rm lab} = 40 \pm 5^\circ$ [35] (full squares; upper lines). The dotted lines are obtained from CBUU calculations without baryon and kaon potentials, the dashed lines show the results with baryon potentials included, while the solid lines correspond to calculations including both nucleon and kaon potentials.

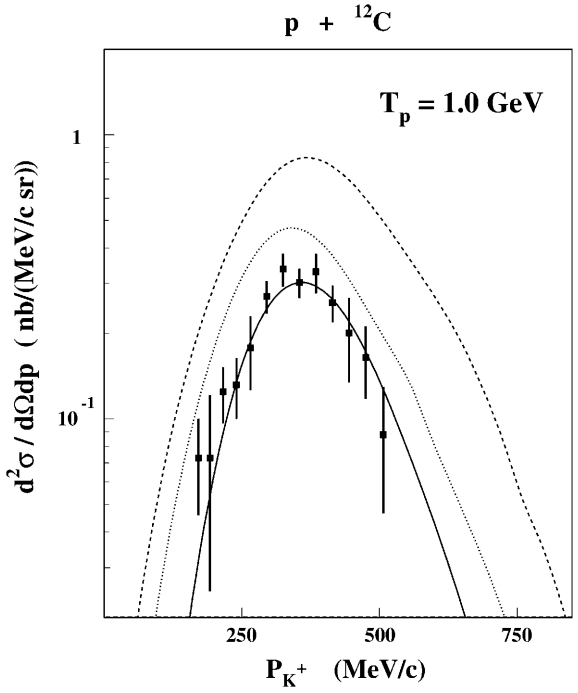

Fig. 9. The calculated differential K^+ spectra for p + C at 1.0 GeV for $\theta_{\rm lab} \leq 12^\circ$ within the acceptance of the ANKE spectrometer in comparison to the data from [38]. The dotted line is obtained from CBUU calculations without baryon and kaon potentials, the dashed line shows the results with baryon potentials included, while the solid line corresponds to calculations including both nucleon and kaon potentials.

target only a fraction of the high-energy pions rescatters in the target and produces K^+Y pairs. Moreover, the role of the secondary channels decreases with increasing kaon momentum such that the high-momentum K^+ tail of the spectra is dominated by the first-chance pN production channel as found out before by Paryev [58].

Furthermore, it is worth to point out that the contribution of the primary channel $pN \to K^+YN$ is enhanced by up to a factor of 3 within the angular range of $\theta \leq 12^\circ$ as compared to the angle integrated yield at the energy $T_{\rm lab} = 1.0$ GeV. Thus, the experimental mass dependence, when expressed in terms of a scaling $\sim A^\alpha$, does not allow to disentangle the relative contribution of the different reaction channels in a satisfying manner for narrow cuts in the K^+ angular distribution.

In order to provide some guideline for extrapolations between experiments measuring K^+ spectra at different angles in the laboratory, we show in fig. 10 the angular distribution of the kaons for momenta $0.2\,{\rm GeV}/c \leq p_K \leq 0.5\,{\rm GeV}/c$ as calculated within the extended CBUU approach for both, baryon and kaon potentials for p + ^{12}C at $T_{\rm lab} = 1.0$, 1.2, 1.5, 1.8, 2.0 and 2.3 GeV. These angular distributions are rather flat within the angular acceptance of the ANKE spectrometer of $\sim 12^\circ$, however, drop substantially for angles larger than 40°. Thus, our calculations (cf. also fig. 9) do not support the idea of a "thermal" production mechanism for kaons in case of $p + A$ reactions.

4 Summary

In this work we have studied the production of K^+-mesons in proton-nucleus collisions from 1.0 to 2.5 GeV with respect to one-step nucleon-nucleon and two-step Δ-nucleon or pion-nucleon production channels on the basis of a coupled-channel transport approach (CBUU) including differential transition probabilities from πN reactions that have been calculated within the folding model (subsect. 2.5). We have included the kaon final-state interactions, which are important for heavy targets like Au or Pb, and explored the effects of momentum-dependent potentials for the nucleon, hyperon and kaon in the nucleus. A comparison of the calculations to the experimental K^+ spectra taken at LBL Berkeley, SATURNE, CELSIUS, GSI and COSY-Jülich has shown that the different data sets are not compatible with each other. Thus no clear signal on in-medium potentials could be extracted from our analysis in comparison to experimental spectra so far.

However, the detailed calculations demonstrate that precise and complete spectra show a substantial sensitivity to the potentials and their momentum dependence.

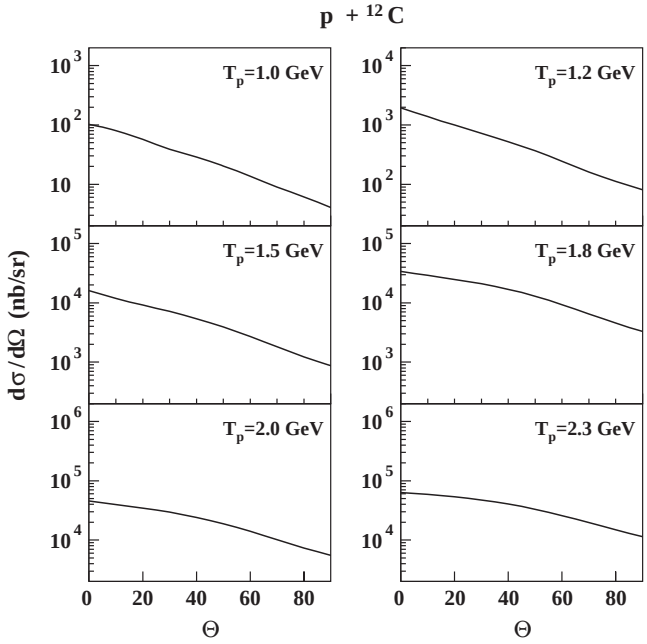

Fig. 10. The calculated angular distribution of the K^+ spectra for p + C at 1.0, 1.2, 1.5, 1.8, 2.0 and 2.3 GeV for $0.2 \leq p_K \leq 0.5\,\mathrm{GeV}/c$. The solid lines are obtained from CBUU calculations including both nucleon and kaon potentials.

At low bombarding energies of $\sim 1.0\,\mathrm{GeV}$ the net attractive potentials for the nucleon and the Λ-hyperon in the final state lead to a relative enhancement of the K^+ spectra while at higher bombarding energies ($\sim 2\,\mathrm{GeV}$) the baryon potentials are repulsive and thus suppress K^+ production relative to the free case. This phenomenon should be seen in the excitation function of the K^+ cross-section when varying T_{lab} from 1.0 to 2.5 GeV. Furthermore, the shape of the spectrum for low K^+ momenta in the laboratory is very sensitive to both Coulomb and nuclear kaon potentials, since the kaons are accelerated by both forces when leaving the nuclear environment and propagating to the continuum. The relative strength of this momentum shift in the forward K^+ spectra is proportional to the square root of the sum of both potentials, *i.e.* $\Delta p \approx \sqrt{2M_K(U_{\mathrm{Coul}} + U_K)}$. Thus the K^+ spectral shape at low momenta (or kinetic energies T_K) allows to determine the strength of the K^+ potential from experimental data in an almost model-independent way especially when comparing kaon spectra from light and heavy targets at the same bombarding energy [64] as a function of T_K. Since most of the K^+ spectra measured so far have been taken at higher momenta in the laboratory (except for ref. [38]) this finding opens up interesting perspectives for the ANKE Collaboration at COSY-Jülich, which has performed a systematic study of K^+ production in $p + A$ reactions down to momenta of $150\,\mathrm{MeV}/c$ in the laboratory or $T_K \approx 23\,\mathrm{MeV}$, respectively.

These data are expected to also shed some light on the open issues in the transport calculations, *i.e.*, the $\Delta N \to K^+ + X$ production cross-sections, the in-medium transition rates for the channels $\pi N \to K^+ Y$ and the on-shell assumption for the intermediate pion in secondary kaon production channels.

The authors like to acknowledge valuable discussions with M. Büscher, V. Koptev, M. Nekipelov, E.Ya. Paryev, P. Senger, A. Sibirtsev, H. Ströher and C. Wilkin on various issues of this study. Financial support has been provided by the German BMBF under grant WTZ-POL 99/001 and the Polish State Committee for Scientific Research under grant 2 P03B 101 19.

References

1. P. Grimm, E. Grosse, Prog. Part. Nucl. Phys. **15**, 339 (1985).
2. P. Braun-Munzinger, J. Stachel, Annu. Rev. Nucl. Part. Sci. **37**, 1 (1987).
3. H. Nifenecker, J.A. Pinston, Prog. Part. Nucl. Phys. **23**, 271 (1989).
4. J. Randrup, C.M. Ko, Nucl. Phys. A **343**, 519 (1980); **411**, 537 (1983).
5. J. Cugnon, R.M. Lombard, Nucl. Phys. A **422**, 635 (1984).
6. S.V. Efremov, M.V. Kazarnovsky, E.Ya. Paryev, Z. Phys. A **344**, 181 (1992).
7. V.I. Komarov *et al.*, Nucl. Phys. A **326**, 397 (1979).
8. M.M. Nesterov, N.A. Tarasov, Sov. Phys. JETP **59**, 226 (1984).
9. N.A. Tarasov, V.P. Koptev, M.M. Nesterov, Pis'ma Zh. Eksp. Teor. Fiz. **43**, 217 (1986).
10. H. Müller, Z. Phys. A **339**, 409 (1991); H. Müller, K. Sistemich, Z. Phys. A **344**, 197 (1992).
11. J. Cugnon, P. Deneye, J. Vandermeulen, Phys. Rev. C **41**, 1339 (1990).
12. A. Sibirtsev, M. Büscher, Z. Phys. A **347**, 191 (1994).
13. S. Teis, W. Cassing, T. Maruyama, U. Mosel, Phys. Lett. B **319**, 47 (1993).
14. Yu.T. Kiselev *et al.*, J. Phys. G **25**, 381 (1999).
15. M. Büscher *et al.*, Phys. Rev. C **65**, 014603 (2001).
16. J. Aichelin, C.M. Ko, Phys. Rev. Lett. **55**, 2661 (1985).
17. W. Cassing *et al.*, Phys. Lett. B **238**, 25 (1990).
18. W. Cassing *et al.*, Z. Phys. A **349**, 77 (1994).
19. W. Cassing, V. Metag, U. Mosel, K. Niita, Phys. Rep. **188**, 363 (1990).
20. V.P. Koptev *et al.*, Sov. Phys. JETP **67**, 2177 (1988).
21. D.B. Kaplan, A.E. Nelson, Phys. Lett. B **175**, 57 (1986).
22. W. Cassing, E.L. Bratkovskaya, Phys. Rep. **308**, 65 (1999).
23. Bao-An Li, A.T. Sustich, Bin Zhang, C.M. Ko, Int. J. Mod. Phys. E **10**, 267 (2001).
24. G.E. Brown, M. Rho, Phys. Rev. Lett. **66**, 2720 (1991).
25. A.E. Nelsen, D. Kaplan, Phys. Lett. B **192**, 193 (1987).
26. J. Schaffner-Bielich, I.N. Mishustin, J. Bondorf, Nucl. Phys. A **625**, 325 (1997).
27. G.E. Brown, C.M. Ko, Z.G. Wu, L.H. Xia, Phys. Rev. C **43**, 1881 (1991).
28. T. Muto, Nucl. Phys. A **691**, 447 (2001).
29. P.K. Sahu, A. Ohnishi, Nucl. Phys. A **691**, 439 (2001).
30. A. Gal, Nucl. Phys. A **691**, 268 (2001).
31. M. Lutz, Phys. Lett. B **426**, 12 (1998).
32. A. Ramos, S. Hirenzaki, S.S. Kamalov, T.T.S. Kuo, Y. Okumura, E. Oset, A. Polls, H. Toki, L. Tolos, Nucl. Phys. A **691**, 259 (2001).

33. A. Sibirtsev, W. Cassing, Nucl. Phys. A **641**, 476 (1998).
34. S. Schnetzer *et al.*, Phys. Rev. C **40**, 640 (1989).
35. M. Debowski *et al.*, Z. Phys. A **356**, 313 (1996).
36. A. Badala *et al.*, Phys. Rev. Lett. **80**, 4863 (1998).
37. S. Barsov *et al.*, Nucl. Instrum. Methods Phys. Res. A **462**, 364 (2001).
38. V. Koptev *et al.*, Phys. Rev. Lett. **87**, 022310 (2001).
39. Gy. Wolf *et al.*, Nucl. Phys. A **517**, 615 (1990); **552**, 549 (1993).
40. Z. Rudy *et al.*, Z. Phys. A **354**, 445 (1996).
41. Ye.S. Golubeva, L.A. Kondratyuk, W. Cassing, Nucl. Phys. A **625**, 832 (1997).
42. W. Cassing *et al.*, Nucl. Phys. A **614**, 415 (1997).
43. K. Weber *et al.*, Nucl. Phys. A **539**, 713 (1992); T. Maruyama *et al.*, Nucl. Phys. A **573**, 653 (1994).
44. W. Ehehalt, W. Cassing, Nucl. Phys. A **602**, 449 (1996).
45. W. Cassing, Nucl. Phys. A **700**, 618 (2002).
46. W. Cassing, E.L. Bratkovskaya, S. Juchem, Nucl. Phys. A **674**, 249 (2000).
47. S. Hama *et al.*, Phys. Rev. C **41**, 2737 (1990).
48. W. Botermans, R. Malfliet, Phys. Rep. **198**, 115 (1990).
49. T. Waas, N. Kaiser, W. Weise, Phys. Lett. B **379**, 34 (1996).
50. B.J. Ver West, R.A. Arndt, Phys. Rev. C **25**, 1979 (1982).
51. K. Tsushima, S.W. Huang, A. Faessler, J. Phys. G **21**, 33 (1995); Phys. Lett. B **337**, 245 (1994).
52. J.T. Balewski *et al.*, Phys. Lett. B **420**, 211 (1998).
53. H. Schopper (Editor), *Landolt-Börnstein, New Series*, Vol. **I/12** (Springer-Verlag, 1988).
54. W. Zwermann, Mod. Phys. Lett. A **3**, 251 (1988).
55. A. Sibirtsev, W. Cassing, nucl-th/9904046.
56. P. Moskal *et al.*, Phys. Lett. B **482**, 356 (2000).
57. A. Sibirtsev, W. Cassing, U. Mosel, Z. Phys. A **358**, 357 (1997).
58. E.Ya. Paryev, Eur. Phys. J. A **5**, 307 (1999).
59. I. Sick, S. Fantoni, A. Fabrocini, O. Benhar, Phys. Lett. B **323**, 267 (1994).
60. E. Vercellin *et al.*, Nuovo Cimento A **106**, 861 (1993).
61. E.Ya. Paryev, Eur. Phys. J. A **9**, 521 (2000).
62. E.Ya. Paryev, preprint INR - 1062/2001.
63. W. Scheinast, for the KaoS Collaboration, Acta. Phys. Pol. B **31**, 2305 (2000).
64. S. Barsov *et al.*, Acta Phys. Pol. B **31**, 2159 (2000).